Supplementary Information

Solar light selective-harvesting eco-friendly colloidal quantum dots for transparent luminescent solar concentrators

Lei Jin,*[a, b, c] Ehsan Hamzehpoor,[c] Jiabin Liu,[b] Xin Liu,[b] Daniele Benetti,[b,c] Gurpreet Singh Selopal,[b] Dmytro F. Perepichka,*[c] Zhiming M. Wang,*[a] Federico Rosei*[b,e]
a Institute of Fundamental and Frontier Sciences, University of Electronic Science and Technology of China, Chengdu, 610054, P. R. China
b Centre for Energy, Materials and Télecommunications, Institut national de la recherche scientifique, 1650 Boul. Lionel-Boulet, Varennes, QC, J3X 1P7, Canada
c Department of Chemistry, McGill University, 801 Sherbrooke Street West, Montreal, Quebec H3A 0B8, Canada
d Institute for Advanced Study, Chengdu University, Chengdu, Sichuan, 610106, P.R. China
e Department of Chemical and Pharmaceutical Sciences, University of Trieste, Via Giorgeri 1, 34127 Trieste (Italy)
Email: jin.jin@mail.mcgill.ca; dmytro.perepichka@mcgill.ca; zhmwang@uestc.edu.cn; federico.rosei@inrs.ca

Experimental Section

Materials

Copper(I) iodide (CuI, 99.999%, powder), Gallium(III) iodide (GaI_3, 99.99%, powder), oleylamine (OLA, technical grade, 70%), 1-dodecanethiol (DDT, ≥98%), sulfur (S, 99.998%, powder), 1-octadecene (ODE, technical grade, 90%), zinc acetate ($Zn(OAc)_2$, 99.99%, powder), oleic acid (OA, technical grade, 90%), zinc stearate ($Zn(St)_2$, 99.99%, powder), Silver(I) acetate (Ag(Ac), ≥99.99%, trace metals basis), Indium(III) acetate ($In(Ac)_3$, 99.99%, trace metals basis), Trioctylphosphine (TOP, 97%), toluene, ethanol, methanol, acetone, lauryl methacrylate (LMA), ethylene glycol dimethacrylate (EGDM), and diphenyl(2,4,6-trimethylbenzoyl)phosphine oxide were purchased from Sigma-Aldrich. All the above chemicals and solvents were used as received without further purification.

Synthesis of CGS/ZnS QDs

Eco-friendly CGS/ZnS QDs were synthesized by modifying a previously reported facile colloidal one-pot core/shell preparation method.[1] All the synthetic procedures were carried out using a Schlenk line system. All the reaction vials of solution stocks were initially placed on a hotplate and degassed through a vacuum line in Schlenk system at 125 °C for 30 min to remove O_2 and

humidity before increasing their temperatures. Three stock solutions of sulfur (S), $Zn(OAc)_2$, and $Zn(St)_2$ were prepared in advance:

The S stock solution was obtained by dissolving 2 mmol of S in 2 mL of ODE at 190 °C for 20 min.

The $Zn(OAc)_2$ stock solution was prepared by dissolving 0.554 g of $Zn(OAc)_2$ in 4 mL of OA, 2 mL of DDT, and 2 mL of ODE at 190 °C for 15 min.

The $Zn(St)_2$ stock solution was obtained by dissolving 8 mmol of $Zn(St)_2$ in 4 mL of DDT and 8 mL of ODE at 250 °C for 60 min.

In a typical synthesis, 11.9 mg of CuI, 225.22 mg of GaI_3, 5 mL of OLA, and 0.5 mL of DDT were loaded into a 50 mL three-neck flask. The mixture was heated to 125 °C with continuous stirring under N_2-purging, then degassed under a vacuum of 100 mTorr for 30 min to form a clear solution. Subsequently, S stock solution was swiftly injected into the three-neck flask at 180 °C under N_2 flow and kept at this temperature for 4 min to allow the growth of $CuGaS_2$ core. For the growth of the ZnS shell, without any intermediate purification steps for the core, the $Zn(OAc)_2$ stock solution was slowly dropped into the vigorously stirring core mixture at 210 °C and held for 30 min under nitrogen flow. Subsequently, the second $Zn(St)_2$ stock solution was slowly injected into the crude mixture at 230 °C and maintained growth for 60 min to obtain the $CuGaS_2$/ZnS QDs. Finally, the solution was left to cool to room temperature. The as-synthesized QDs were purified at least three times with an excess amount of ethanol (centrifuged at 6000 rpm for 15 min) and finally re-dispersed in toluene for future usage. The reaction scheme is illustrated in **Figure S1** below.

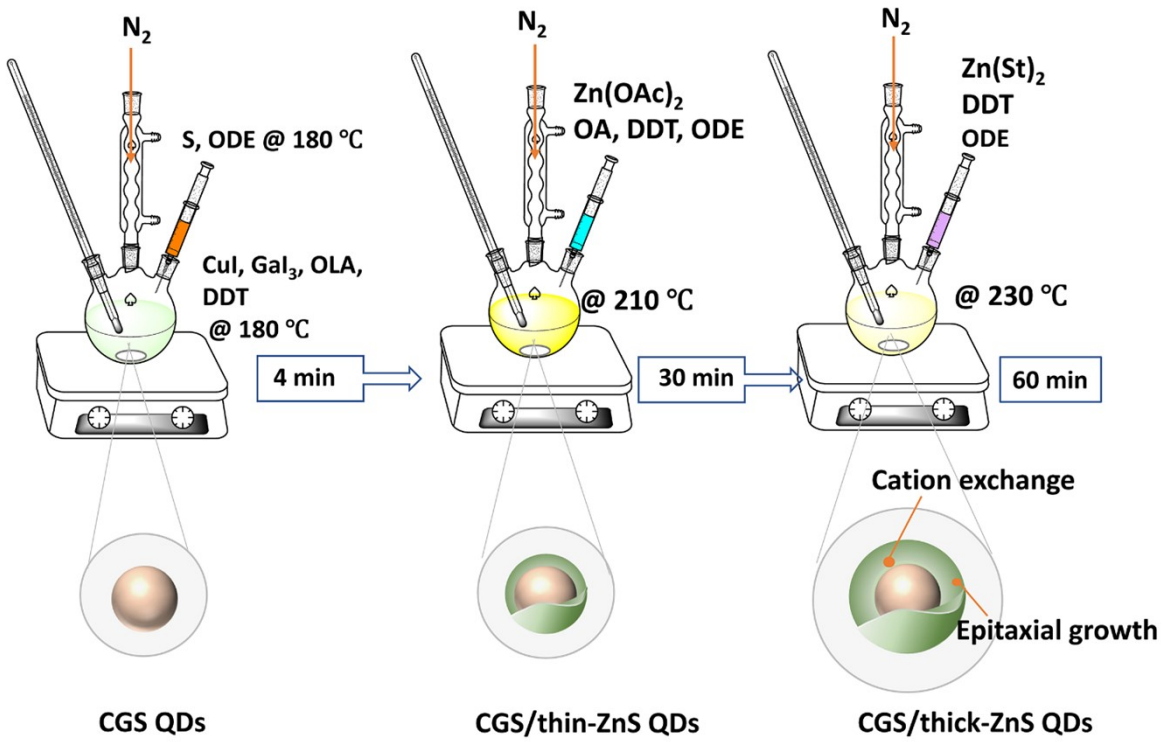

Figure S1. Synthetic scheme for the preparation of CGS/ZnS QDs.

Synthesis of AIS/ZnS QDs.

The $AgInS_2$/ZnS QDs were synthesized using a wet colloidal one-pot core/shell synthesis method which was adapted from previous studies[2, 3] with slight modifications. Before synthesis of QDs, three stock solutions of S, $Zn(OAc)_2$, and $Zn(St)_2$ were prepared. All the synthetic procedures were carried out using a Schlenk line system.

The S-DDT stock solution: a mixture containing 1.1 mmol of sulfur powder and 1.6 g OA and 6.6 mL of DDT was sonicated until all sulfur had dissolved (~ 30 min) and then purged with nitrogen for ~30 min.

The $Zn(St)_2$ stock solution: 0.4 mmol $Zn(Str)_2$, 0.4 mmol sulfur powder, and 2 mL TOP were mixed and degassed for 30 min in a 20 mL three-neck flask. The mixture was heated to 100 ℃ to obtain a transparent liquid as a shell formation precursor.

In a typical synthesis, 0.53 mmol of Ag(Ac), 0.51 mmol of $In(Ac)_3$ and 20 mL of DDT were combined in a 50 mL three-neck flask, degassed at 90 ℃ for 30 min and stirred under N_2 purging at 150 ℃ for 1 hour. The S-DDT stock solution was then rapidly injected into the flask containing the silver, indium, and DDT precursors at 150 ºC. The reaction was allowed to proceed for 10 min for the nucleation and growth of AIS QDs. For the growth of the ZnS shell on the surface of the

AIS core, without any intermediate purification steps for the core, the $Zn(St)_2$ stock solution was slowly injected into the crude solution at 150 ºC and maintained to grow for 60 min. The flask was rapidly cooled with ice water, at which point the reaction was finally quenched. OA (~1 mL) was added to the flask at ~40 °C, after which point the flask continued to cool to room temperature. The as-synthesized AIS/ZnS QDs were purified twice with ethanol, methanol, and acetone, and re-dispersed in toluene for future usage.

Fabrication of QD-based LSC

The polymer matrix based LSCs were fabricated according to previous work.[4, 5] Typically, the solvent of QDs (toluene) was pumped away from the QD-solution under inert N_2 atmosphere until a QD slurry was obtained. Full polymer LSCs are produced by pouring the polymer solution containing the luminophores into pre-made molds. Subsequently, the solution can be solidified into its final form through UV-light polymerization. A mixture of monomer LMA and 20 wt% cross-linking agent EGDM and a 0.1 wt% diphenyl(2,4,6-trimethyl benzoyl)phosphine oxide (UV initiator) was sonicated until a clear solution was obtained. The obtained mixture was injected into the flask containing the solvent-free QDs. After ultrasound treatment, a homogeneous mixture was obtained and injected into a mold consisting of two glass slides separated by a flexible silicon rubber spacer with a thickness of 2.0 mm. The filled mold was kept under UV (~400 nm) illumination for 1 h.

After the LSCs were completely dry (thickness ~2 mm), one mono-crystalline Si PV strip (Vikocell Solar) was mounted on one of the LSC edges and the remaining three edges were covered with black tapes to block the light and internal light reflection. For tandem LSCs, CGS/ZnS and AIS/ZnS QD-based LSCs were encapsulated together by epoxy around the edges, where an air gap thickness is ~0.5 mm.

Characterization

Transmission electron microscopy (TEM) images and energy-dispersive X-ray spectroscopy (EDS) elemental mapping of QDs were obtained by using JEOL 2100F TEM system. X-ray diffraction (XRD) in a 2θ range of 10°-70° was recorded to reveal the crystal structure of QDs, which was conducted using a Panalytical X-Pert PRO MRD operated at 40 kV and 40 mA with a Ni-filtered Cu Ka radiation (λ=1.541 A) source. The size of QD can be calculated via Scherrer's formula

$$D = \frac{0.94\lambda}{\beta cos\theta}$$ **(Equation S1)**

where D is the mean size of crystalline domains in nm, λ is the X-ray wavelength (0.154 nm). θ is the half Bragg's angle in radians. Instead of using the full width at half maxima (FWHM) from XRD peaks, we employed the internal breadth of XRD (represented as β in radians, obtained by dividing the integrated area under XRD peak by its height) to achieve independence from the shape of Bragg peaks, especially the asymmetrical shape.

X-ray photoelectron spectroscopy (XPS) was performed on a VG Escalab 220i-XL equipped with an Al Ka source. The C 1s peak (calibrated to a binding Energy=284.6 eV) was used as an intrinsic reference to rule out charging effects. Ultraviolet photoelectron spectroscopy (UPS) measurements were performed on a VG ESCALAB 3 Mark II high vacuum system with He I radiation (21.21 eV). Absorption spectra, reflectance (R(λ)) and specular transmittance were collected through Varian Cary 5000 UV-vis-NIR spectrophotometer (Varian). Photoluminescence (PL) spectra and PL lifetime of the QDs in solution or polymer were obtained by Fluorolog-3 system (Horiba Jobin Yvon). Steady-state photoluminescence spectra were collected using a Fluorolog-3 fluorometer from Horiba Jobin-Yvon. Absolute Photoluminescent Quantum yield measurements of the QDs in solution or the polymer were performed with a Quanta-φ integrating sphere from Horiba Scientific. The emission lifetimes of the samples were determined by the Time-Correlated Single Photon Counting (TCSPC) technique (<1μs) and fast multichannel scaler mode (fast MCS; <1ms) using a 373 nm Delta Diode and 273 nm Spectra LED pulsed laser diodes controlled via a DeltaHub controller, both from Horiba Scientific.

The average PL lifetime can be calculated as follows:[6, 7]

$$< \tau >= \frac{\sum a_i \tau_i^2}{\sum a_i \tau_i}$$ (**Equation S2**)

where a_i is the fitting coefficients of PL decay and τ_i represent the characteristic lifetimes (i= 1, 2, 3).

To assess aesthetic quality, we calculated the average visible transmittance (AVT), the color rendering index (CRI), and the coordinates (a*, b*) in the CIELAB color space.[8] The average visible transparency (AVT[8, 9]) was calculated based on the transmittance of LSC (T), the visual

perception of human eyes through the photonic response (P), and the solar photon flus (S) in AM 1.5G:[8, 10]

$$AVT = \frac{\int T(\lambda)P(\lambda)S(\lambda)d\lambda}{\int P(\lambda)S(\lambda)d\lambda} \quad \textbf{(Equation S3)}$$

Using McCamy's approximation algorithm,[11] the correlated color temperature (CCT) can be verified:

$$CCT = -449n^3 + 3525n^2 - 6823.3n + 5520.33 \quad \textbf{(Equation S4)}$$

where $n = \frac{x - 0.3320}{y - 0.1858}$.

A compact Solar Simulator AAA (Sciencetech SLB- 300A) and a Keysight 2900A SourceMeter were used to measure the photocurrent density-voltage and photocurrent density-time curves (at a bias scan rate of 35 mV/s) under simulated sunlight (1 Sun = AM 1.5G, 100 mW/cm^2). To verify the one-sun illumination, a Si reference diode (Sciencetech) was used to adjust the distance (~30 cm) between solar simulator and LSC before each measurement. Since the solar cell is only used on a single edge of the LSC, the overall LSC performance needs to be multiplied by a factor of four to account for the entire structure. The current density of LSC-PV was normalized over the surface area of the LSC:[12]

$$J_{SC}^{LSC} = \frac{I_{SC}^{LSC} \times 4}{LSC_{top}} \quad \textbf{(Equation S5)}$$

where I_{SC}^{LSC} is the short circuit current from the Si solar cell with one LSC, LSC_{top} is the top area of the LSC.

The power conversion efficiency (PCE) of LSC-PV can be calculated using the following formula:[12, 13]

$$PCE_{LSC-PV} = \frac{J_{SC}^{LSC} \times FF \times V_{oc}}{P_0} \times 4 \times 100\% \quad \textbf{(Equation S6)}$$

where FF is the fill factor, V_{OC} is the open-circuit voltage, and P_0 is the integrated solar power density (100 mW/cm^2 for AM 1.5G).

For better comparison, we also calcualted the optical efficiency (η_{opt}), which is defined as the proportion between the output power (P_{out}) obtained from the edges of the LSC and the input power (P_{in}) entering through the top surface of the LSC. When calibrated PV cells are utilized to examine the optical performance of LSCs, η_{opt} is defined as follows:[14]

$$\eta_{opt} = \frac{I_{SC}^{LSC}}{I_{SC}^{PV} \times G} \quad \textbf{(Equation S7)}$$

Where I_{SC}^{PV} is the short-circuit current from a Si PV cell under direct solar illumination. G is the geometric factor, which is the ratio of the top surface area of the LSC to the surface area of all the edges.

To ensure uniformity in our analysis, we employed the external photon efficiency ($\boldsymbol{\eta_{ext}}$), which shares a similar definition with η_{opt}. $\boldsymbol{\eta_{ext}}$ quantifies the ratio of the total emitted photons that reach the device edge to the total incident solar photons on the front surface, which can be calculated as follows:[14]

$$\eta_{ext} = \frac{\int AM\ 1.5G\ (\lambda)\eta_{ext}(\lambda)d\lambda}{\int AM\ 1.5G\ (\lambda)d\lambda} \quad \textbf{(Equation S8)}$$

$$\eta_{ext}(\lambda) \cong EQE_{LSC}(\lambda) \cdot EQE_{PV} \quad \textbf{(Equation S9)}$$

Where AM 1.5G ($\boldsymbol{\lambda}$) represents the photon flux spectrum in units of number of photons, $\boldsymbol{\eta_{ext(\lambda)}}$ is the proportion of emitted photons with wavelength $\boldsymbol{\lambda}$ that reach the device edges compared to the total solar photons at $\boldsymbol{\lambda}$ incident on the front surface. $\boldsymbol{EQE_{LSC(\lambda)}}$ denotes the EQE of the LSC at the wavelength of $\boldsymbol{\lambda}$, $\boldsymbol{EQE_{PV}}$ is the EQE of the attached solar cell.

To assess the performance of the LSC, we followed recent standards protocol to measure their average external quantum efficiencies (EQE) and matched it with the current density of LSC-PV.[12] A solitary edge of the LSC was completely fitted with a manually cut piece of commercial monocrystalline solar cell (from Vikocell), while the remaining three edges were enclosed by black tapes. The position dependent EQE_{LSC} measurements were performed using Newport Oriel IQE 200.[12] For the LSC with L=50 mm, 5 scans were taken along the centerlines (with mask) and each

EQE spectrum was corrected by multiplying the corresponding geometry factor (g, different definition with g in Equation S7), accounting for the different angle subtended by the edge-mounted PV at various excitation distance (d):[12, 15, 16]

$$g = \frac{2\pi}{2\varphi} = \frac{\pi}{tan^{-1}\left(\frac{L}{2d}\right)} \quad \textbf{(Equation S10)}$$

where L is the length of the LSC and 2φ is the angle facing the PV on the edge. Then the five corrected spectra were averaged to one EQE for the whole LSC.

To verify the measurement's self-consistency, independent measurements of transmittance T(λ), reflectance R(λ) and EQE were combined to check the photon balance at each wavelength, which should satisfy the following inequality relation:

$$EQE_{LSC}(\lambda) + R(\lambda) + T(\lambda) \leq 1 \quad \textbf{(Equation S11)}$$

which indicates $EQE_{LSC}(\lambda) \leq A(\lambda)$, where the absolute light absorption of LSC A(λ)=1-R(λ)-T(λ).

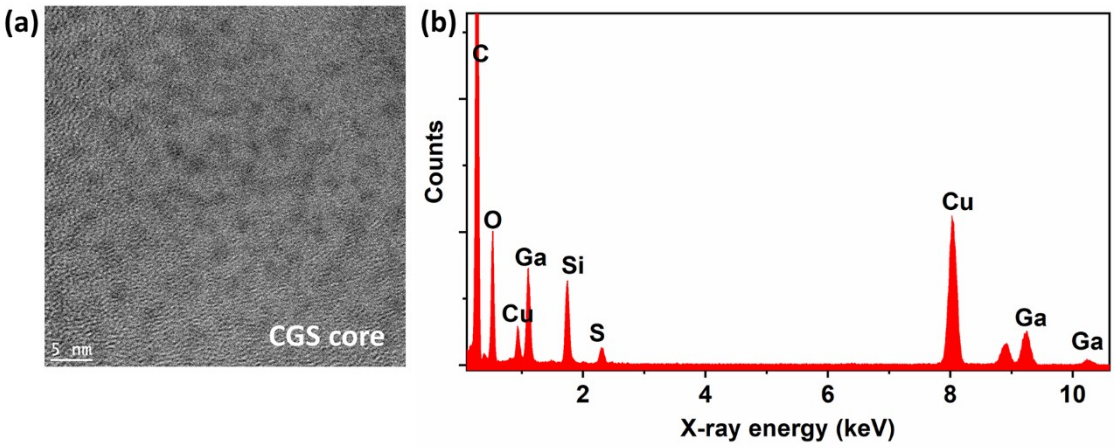

Figure S2. (a)TEM image and (b) EDS spectrum of CGS QDs.

Table S1. Size and shell thickness of as-synthesized QDs calculated from XRD data using Scherrer's formula and TEM.

QD type	2θ (°)	β	Calculated size (nm)	XRD β error	Corrected β	TEM (nm)	ZnS thickness (nm)
CuGaS	29.2	7.0	1.4		6.3	--	--
CuGaS/ZnS	28.9	3.3	2.6	0.7	2.6	3.3	1.0

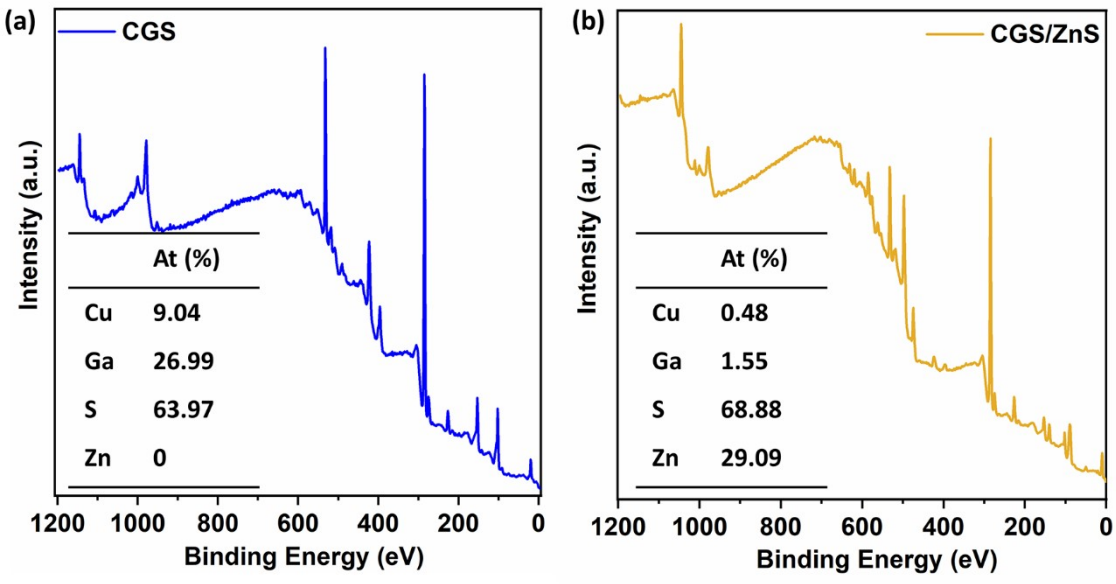

Figure S3. XPS survey scan of (a) CGS and (b) CGS/ZnS QDs. Inset: summary of the atomic ratio CGS and CGS/ZnS QDs from XPS analysis.

Table S2. Summary of the XPS peak position of CGS and CGS/ZnS QDs**.**

QD	Peak Position (eV)							
	Cu		Ga		S		Zn	
	$2p_{1/2}$	$2p_{3/2}$	$2p_{1/2}$	$2p_{3/2}$	$2p_{1/2}$	$2p_{3/2}$	$2p_{1/2}$	$2p_{3/2}$
CGS	952.1	932.3	1144.9	1118.1	162.9	161.7	--	--
CGS/ZnS	952.4	932.5	1144.2	1118.3	163.2	161.9	1045.1	1022.0

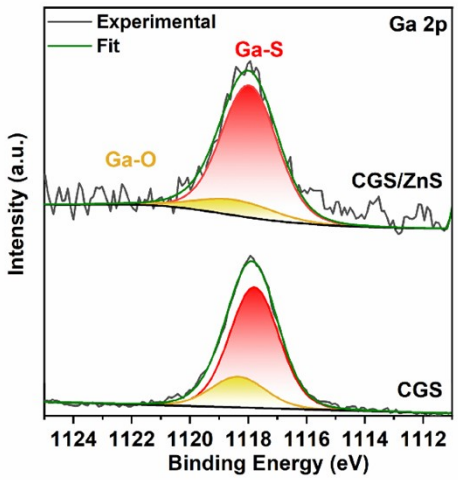

QDs	Ga-O (area%)	Ga-S (area%)
CGS	27.86	72.14
CGS/ZnS	16.47	83.53

Figure S4. The Ga $2P_{3/2}$ core level XPS of CGS and CGS/ZnS QDs.

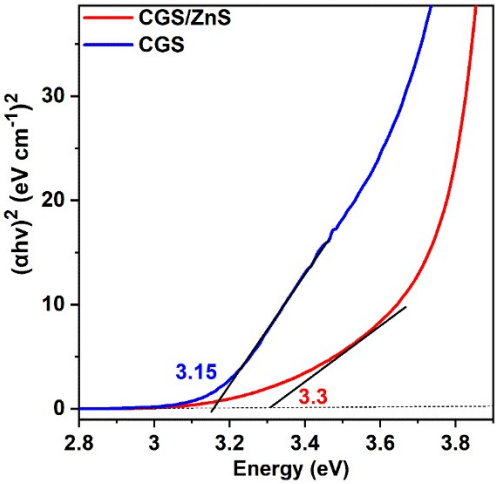

Figure S5. The extrapolation of Tauc plots ($(\alpha hv)^2$) versus photon energy (hv) of CGS and CGS/ZnS QDs.

Table S3. Fitted average PL lifetimes of QDs.

Samples	PL (nm)	τ_1 (ns)	τ_2 (ns)	τ_3 (ns)	α_1 (%)	α_2 (%)	α_3 (%)	τ_{ave} (ns)
CGS	450	2.4	12.6	1.1	34.53	2.72	62.76	3.8
CGS/ZnS	550	7.2	460.1	1.3	7.68	87.46	4.86	459.1

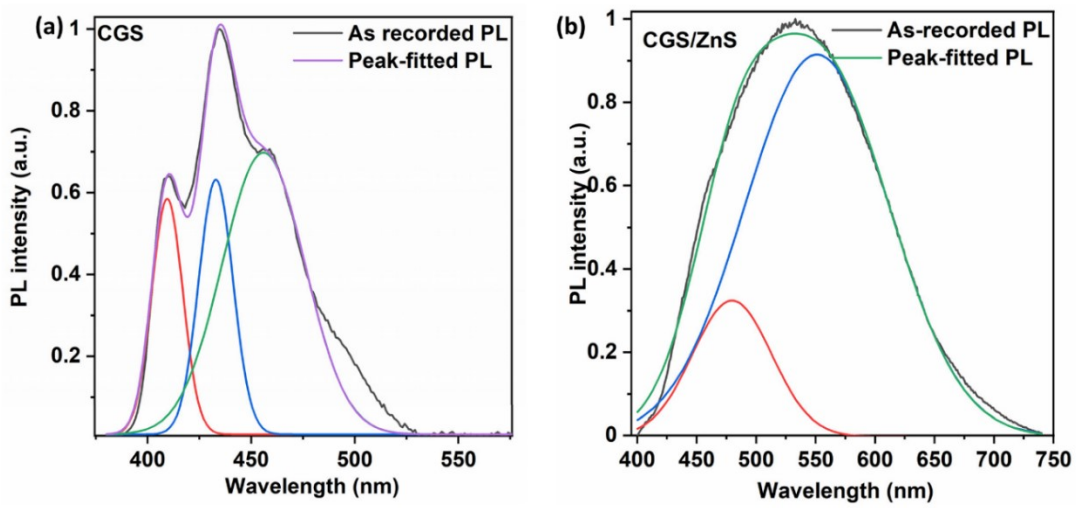

Figure S6. PL spectral decomposition of (a) CGS and (b) CGS/ZnS QDs.

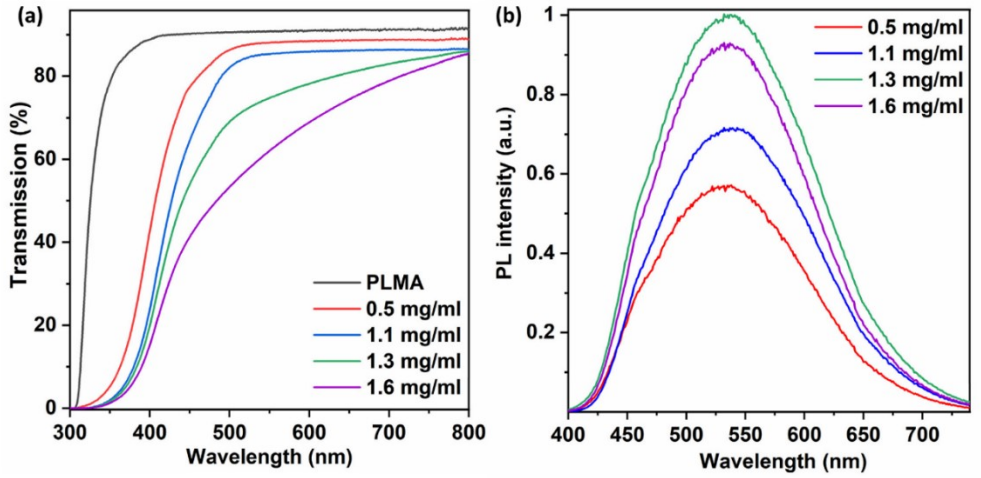

Figure S7. (a) Transmittance spectra and (b) PL spectra of LSCs with various concentrations of CGS/ZnS QDs in PLMA.

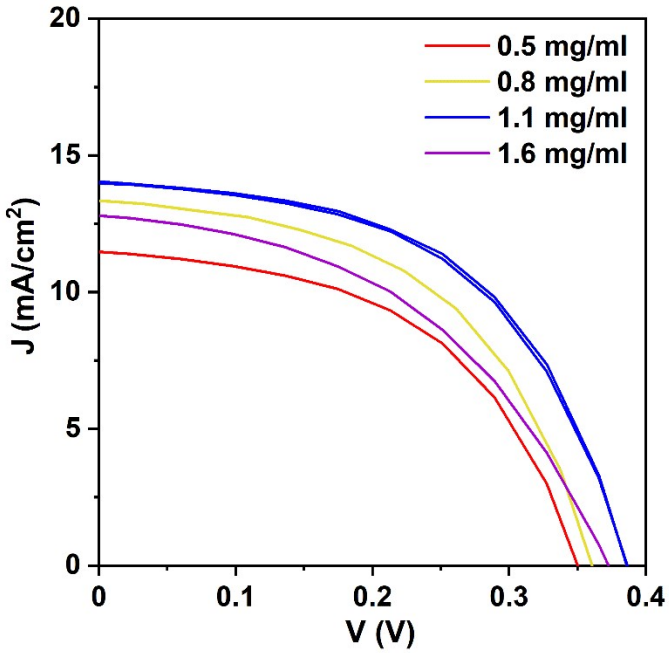

Figure S8. Current density-voltage (J-V) curves of PV with different concentrations of QDs in PLMA solution (mg/ml). The current density was calculated by dividing the area of PV cells and then corrected by multiplying the current density by 4.

Table S4. Photovoltaic parameters obtained from J-V measurement for different QD concentrations.

QD concentration	J_{sc} (mA/cm^2)	J_{sc}^{LSC} (mA/cm^2)*	V_{oc} (V)	FF (%)	PCE (%)
0.5 mg/ml	11.825	0.473	0.350	50.8	0.084
0.8 mg/ml	13.425	0.537	0.351	50.6	0.095
1.1 mg/ml	13.975	0.558	0.388	53.6	0.113
1.6 mg/ml	13.525	0.541	0.373	45.4	0.092

*: The J_{sc} was estimated based on the LSC front surface area of 5 ×5 cm^2. One piece of Si PV cell is couple to one edge of the LSC, thus the current density was corrected by multiplying by 4.

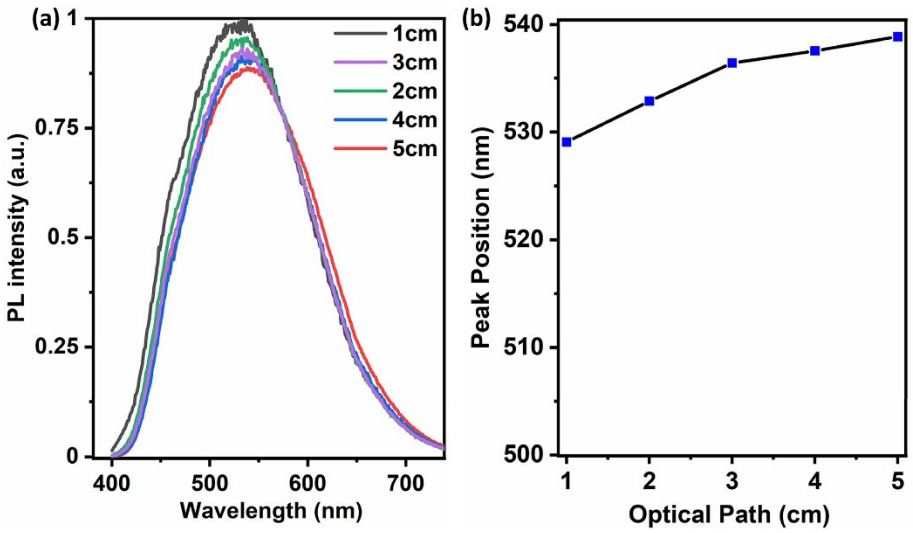

Figure S9. (a) PL spectra measured at different optical paths of LSC. (b) The variation of PL peak position as a function of optical path.

Table S5. CIE 1931 Parameters calculated from PL and transmittance spectra.

	x	y	L*	a*	b*
CGS PL	0.17629	0.19107	59838.05723	-2547.02897	-46310.84128
CGS/ZnS PL	0.32073	0.42025	86593.67314	-26335.05773	25799.6306
CGS/ZnS LSC Transmission	0.37306	0.38947	472.91053	-4.63038	80.87727
PLMA transmission	0.34638	0.35902	505.46749	0.44646	1.68067
AM 1.5G transmission	0.34316	0.36516	100.02558	-4.26107	2.15709

L* refers to lightness, with a and b, the opposite color components of green to red (a*) and blue to yellow (b*).

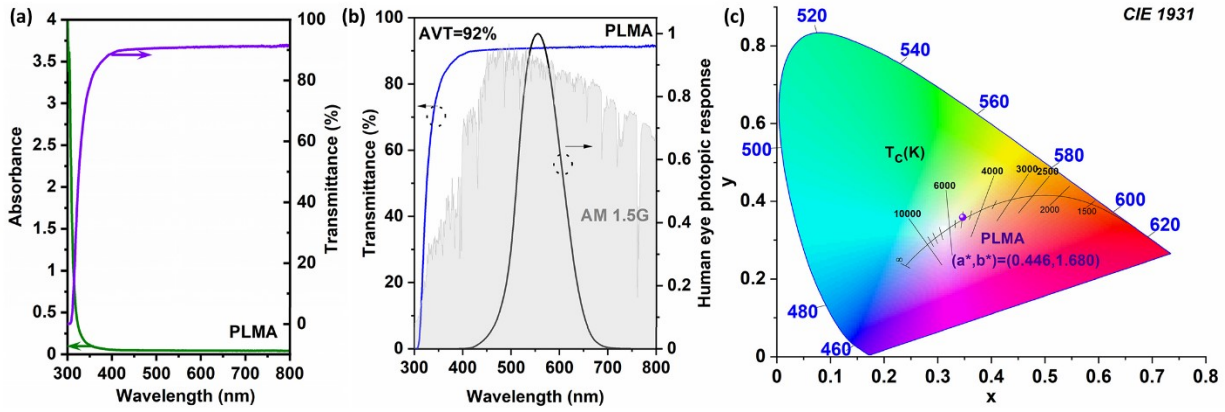

Figure S10. (a) Absorption and transmission spectra, (b) AVT and (c) corresponding CIELAB coordinates of PLMA in the CIE 1931 program. Grey area is AM 1.5G standard spectra.

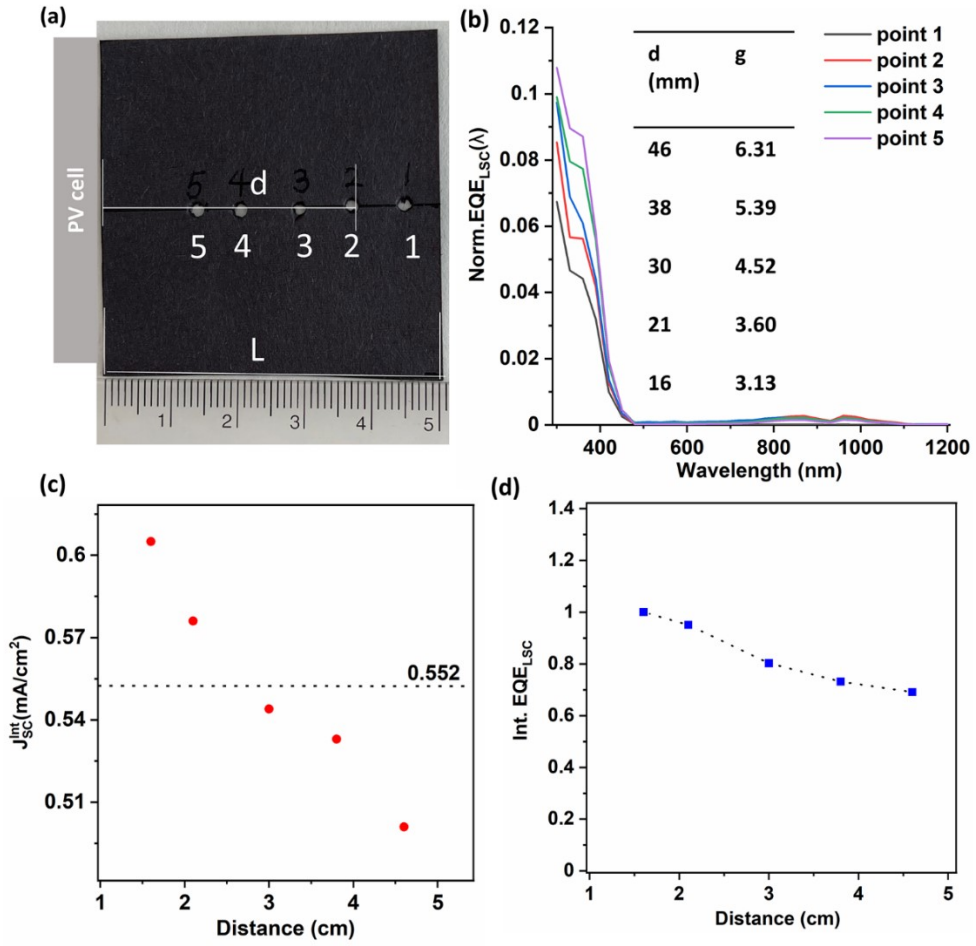

Figure S11. (a) The photo of the mask for EQE measurement of LSC. L is the length of LSC, and d is the distance between the aperture and the edge of LSC. (b) The position dependent EQE spectra of LSC. (c) The variation of EQE at peak position and (d) corresponding *J* with the position.

Table S6. The parameters obtained from J-V measurement.

	J_{sc} (one-PV)[a] (mA/cm^2)	J_{sc}^{LSC} *(mA/cm^2)[b]	V_{oc}(V)	FF(%)	optical efficiency (%)[c]	PCE(%)
PV cell	32	--	0.495	52.6	--	8.33
CGS/ZnS-LSC	3.487	0.558	0.388	53.6	1.7	0.113

[a] J_{sc} was calculated by dividing the photocurrent with the edge area of LSC (LSC_{edge}, under the conditions that one edge of LSC was covered by a PV cell).

[b] J_{sc}^{LSC} was calculated by dividing the photocurrent with the top surface area of LSC (LSC_{top}). $J_{sc}^{LSC} = (J_{sc} \times LSC_{edge} \times 4)/LSC_{top}$

[c] Optical efficiency (%) was calculated based on Equation S8. G=6.25

Table S7. Performance comparison of LSCs based on various UV-active luminophores.

Luminophores	PLQY (%)	Size (cm^3)	AVT (%)	Optical Efficiency (%)	Ref
CGS/ZnS	80	5×5×0.2	75	1.625	This work
$Cs_3Cu_2I_5/CsCu_2I_3$	--	2×3.5×0.5	86.7	1.15	[17]
Mn^{2+}/Yb^{3+} codoped $CsPbCl_3$	125.3	20×20×0.5	--	1.5	[18]
europium(III) doped 4-hydroxy2-methyl-1,5-naphthyridine-3-carbonitrile	68.9	5×5×0.4	90	0.51	[19]
Eu-doped ionosilicas	30	7.6×2.6×0.1	--	0.68	[20]
$MAPbI_3$ Perovskite film	45.8	10×10×0.1	--	2.79	[21]
Bi-doped $Cs_2Ag_{0.4}Na_{0.6}InCl_6$	61.9	10×10×0.2	--	0.7	[22]
Silicon QDs	40	8.3×2.5×0.2	87	--	[23]
$NaI:Tm^{2+}$	33.2	100×100×0.5	80	0.71	[24]
$M_6X_{12}•L_2$	75	2.5×2.5×0.1	84	--	[25]
$CuGaS/ZnS+(dMDAEMA)_4[Re_6S_8(NCS)_6]$	78	2.5×2.5×0.3	80	3.47	[26]
PyPBTM	26	5×5×0.6	--	0.5	[27]
C_8-BTBT-Ox_2-C_8 derivative	95	40×40×0.2	71	3	[28]
carbon nanodots	94	3×3×0.3	--	3.9*	[29]
Si QDs	93	12×12×0.2	86	2.47	[30]
gem-Pyrene Ethenes	46.8	7.5×2.5×0.1	--	1.3	[31]
Dye C1, C6, BO14, KR620, DTDCI	--	4×4×1.2	70	3.6	[32]
$(dMDAEMA)_2[Mo_6I_{14}]$	81.6	2×2×0.3	85	1.24	[33]
Si QDs	60	20×20×0.5	84	1.57	[34]
Si QDs	30.54	10×10×0.2	86	1.18	[35]
$ZnSe:Mn^{2+}/ZnS$ QDs	83.3	7.6×2.6×0.2	83.8	--	[36]
europium(III) (Eu^{3+}) tetrakis(β-diketonate)	62.5	3×3×0.4	89	1.46	[37]

*Estimated by using the light absorbing efficiency the QYs of the luminophores, the trapping efficiency, simulation factor, VT-LSC length and effective absorption coefficient.

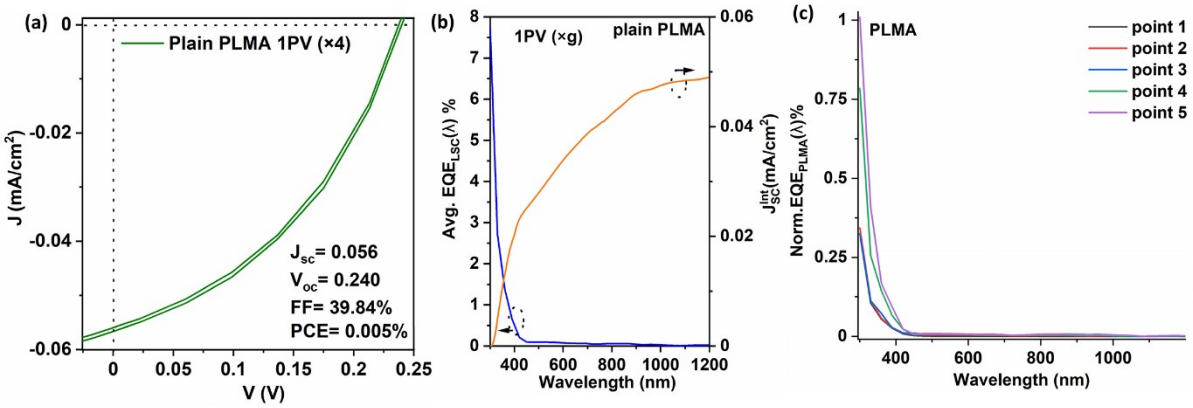

Figure S12. (a) The J-V curve, (b) the EQE and corresponding integrated current density, and (c) the position-dependent EQE spectra of plain PLMA (without QDs). The dimension of plain PLMA is 0.2×5×5 cm^3 (identical to QD-LSC).

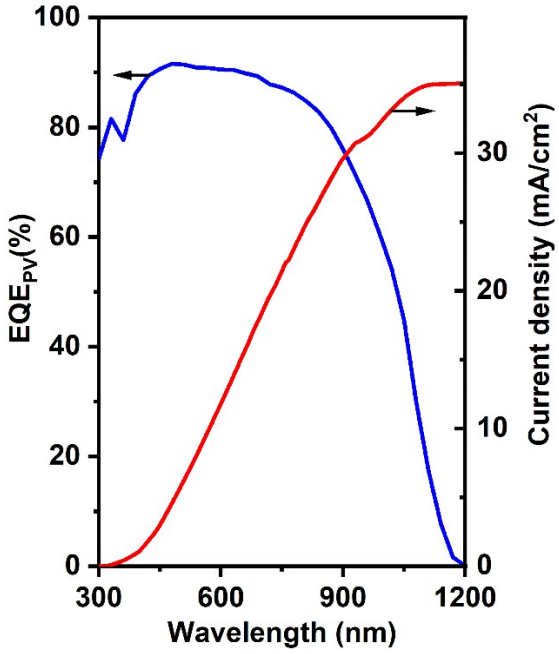

Figure S13. (a) The EQE and corresponding integrated current density of commercial Si solar cell.

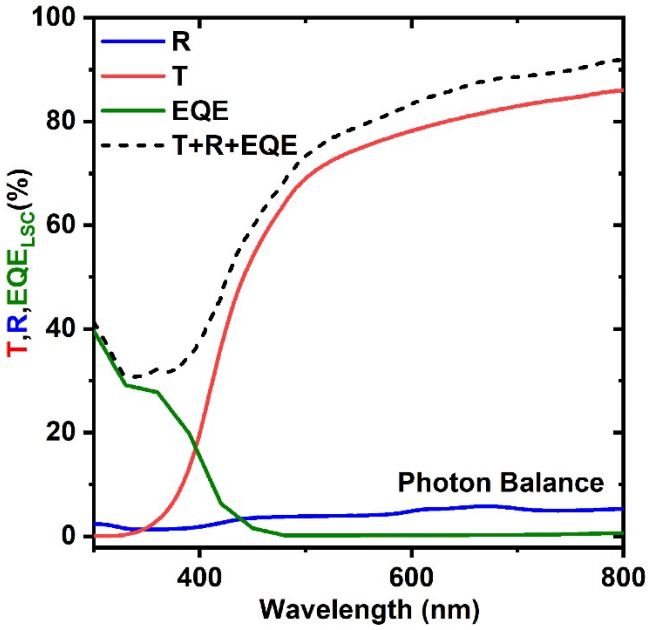

Figure S14. (e) Photon balance check for the CGS/ZnS-based LSC with independent measurements of transmittance T(λ), reflectance R(λ), and EQE.

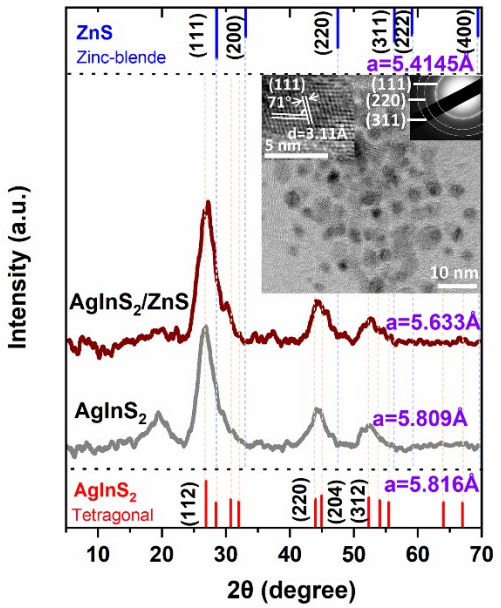

Figure S15. XRD pattern and corresponding SAED patterns (inserted image) of AIS and AIS/ZnS QDs. The high-resolution TEM and XRD show the lattice space of AIS with chalcopyrite structure (tetragonal phase, JCPDS #01-075-0117) and ZnS shell with cubic structure (JCPDS #01-077-2100).

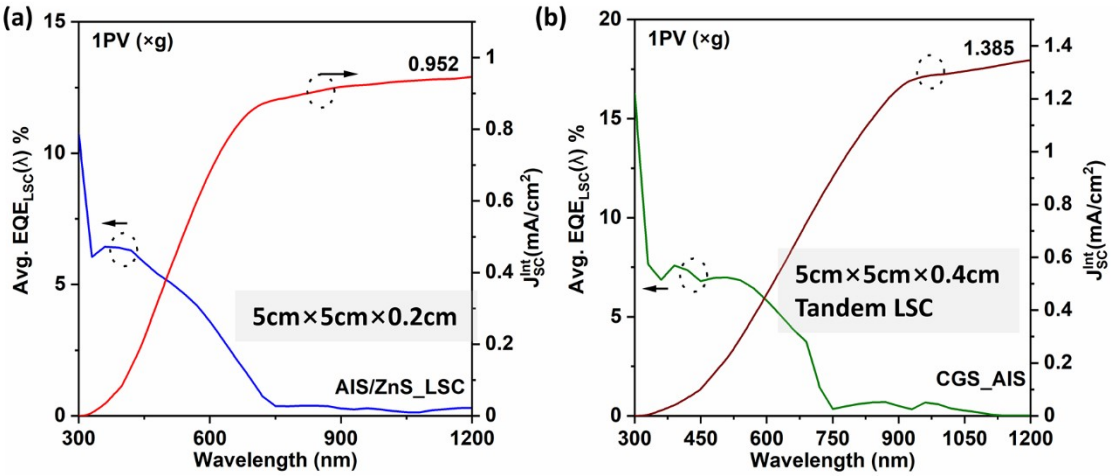

Figure S16. The averaged $EQE_{LSC}(\lambda)$ spectra and integrated current density from EQE spectra of (a) AIS/ZnS single-layer LSC, (b) CGS/ZnS- AIS/ZnS tandem LSC.

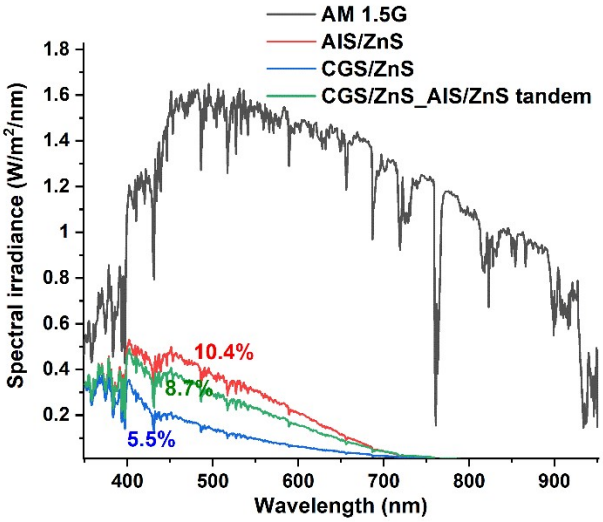

Figure S17. AM 1.5G solar spectrum, absorption, and calculated solar absorption of the CGS/ZnS-LSC, AIS/ZnS-LSC and tandem LSC.

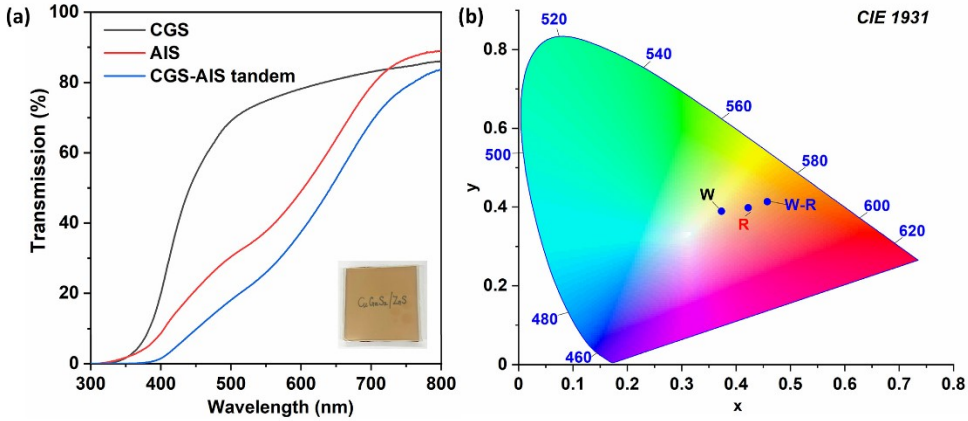

Figure S18. (a) Transmittance spectra and (b) corresponding CIELAB coordinates of CGS/ZnS-LSC (W), AIS/ZnS-LSC (R) and CGS/ZnS-AIS/ZnS tandem LSC (W-R) in the CIE 1931 program.

Table S8. The parameters obtained from J-V measurement for tandem LSC (one PV).

	J_{sc} (one-PV)[a] (mA/cm^2)	J_{sc}^{LSC} *(mA/cm^2)[b]	V_{oc}(V)	FF(%)	optical efficiency (%)[c]	PCE(%)
W-W	6.69	1.07	0.408	53.4	3.35	0.233
W-R	8.89	1.41	0.415	53.6	4.44	0.314
R-R	11.06	1.76	0.406	53.1	5.53	0.379

Table S9. CIE 1931 Parameters and CRI calculated from transmittance spectra.

	x	y	L*	a*	b*	CRI	AVT
CGS/ZnS LSC Transmission	0.37306	0.38947	472.91053	-4.63038	80.87727	91.6	74.8
PLMA transmission	0.34638	0.35902	505.46749	0.44646	1.68067	99.53	90.83
Tandem W-R	0.34316	0.36516	100.02558	-4.26107	2.15709	56.38	29.40

References

1. M. Jalalah, M. S. Al-Assiri and J. G. Park, *Adv. Energy Mater.*, 2018, **8**, 1703418.
2. K. E. Hughes, S. R. Ostheller, H. D. Nelson and D. R. Gamelin, *Nano Lett.*, 2018, **19**, 1318-1325.
3. W. Chen, J. Li, P. Liu, H. Liu, J. Xia, S. Li, D. Wang, D. Wu, W. Lu, X. W. Sun and K. Wang, *Sol. RRL*, 2017, **1**, 1700041.
4. H. Zhao, D. Benetti, X. Tong, H. Zhang, Y. Zhou, G. Liu, D. Ma, S. Sun, Z. M. Wang, Y. Wang and F. Rosei, *Nano Energy*, 2018, **50**, 756-765.
5. X. Liu, B. Luo, J. Liu, D. Jing, D. Benetti and F. Rosei, *J. Mater. Chem. A*, 2020, **8**, 1787-1798.
6. L. Jin, G. Sirigu, X. Tong, A. Camellini, A. Parisini, G. Nicotra, C. Spinella, H. Zhao, S. Sun, V. Morandi, M. Zavelani-Rossi, F. Rosei and A. Vomiero, *Nano Energy*, 2016, **30**, 531-541.
7. R. Adhikari, L. Jin, F. Navarro-Pardo, D. Benetti, B. AlOtaibi, S. Vanka, H. Zhao, Z. Mi, A. Vomiero and F. Rosei, *Nano Energy*, 2016, **27**, 265-274.
8. C. Yang, D. Liu, M. Bates, M. C. Barr and R. R. Lunt, *Joule*, 2019, **3**, 1803-1809.
9. C. J. Traverse, R. Pandey, M. C. Barr and R. R. Lunt, *Nat. Energy*, 2017, **2**, 849-860.
10. W. Naim, V. Novelli, I. Nikolinakos, N. Barbero, I. Dzeba, F. Grifoni, Y. Ren, T. Alnasser, A. Velardo and R. Borrelli, *Jacs Au*, 2021, **1**, 409-426.
11. C. S. McCamy, *Color Research & Application*, 1992, **17**, 142-144.
12. C. Yang, D. Liu and R. R. Lunt, *Joule*, 2019, **3**, 2871-2876.
13. C. Yang, H. A. Atwater, M. A. Baldo, D. Baran, C. J. Barile, M. C. Barr, M. Bates, M. G. Bawendi, M. R. Bergren, B. Borhan, C. J. Brabec, S. Brovelli, V. Bulović, P. Ceroni, M. G. Debije, J.-M. Delgado-Sanchez, W.-J. Dong, P. M. Duxbury, R. C. Evans, S. R. Forrest, D. R. Gamelin, N. C. Giebink, X. Gong, G. Griffini, F. Guo, C. K. Herrera, A. W. Y. Ho-Baillie, R. J. Holmes, S.-K. Hong, T. Kirchartz, B.

G. Levine, H. Li, Y. Li, D. Liu, M. A. Loi, C. K. Luscombe, N. S. Makarov, M. Fahad, R. Mazzaro, H. McDaniel, M. D. McGehee, F. Meinardi, A. Menéndez-Velázquez, J. Min, D. B. Mitzi, M. Moemeni, J. H. Moon, A. Nattestad, M. K. Nazeeruddin, A. F. Nogueira, U. W. Paetzold, D. L. Patrick, A. Pucci, B. P. Rand, E. Reichmanis, B. S. Richards, J. Roncali, F. Rosei, T. W. Schmidt, F. So, C.-C. Tu, A. Vahdani, W. G. J. H. M. v. Sark, R. Verduzco, A. Vomiero, W. W. H. Wong, K. Wu, H.-L. Yip, X. Zhang, H. Zhao and R. R. Lunt, *Joule*, 2022, **6**, 8-15.

14. Y. Zhou, H. Zhao, D. Ma and F. Rosei, *Chem. Soc. Rev.*, 2018, **47**, 5866-5890.
15. M. J. Currie, J. K. Mapel, T. D. Heidel, S. Goffri and M. A. Baldo, *Science*, 2008, **321**, 226-228.
16. J. S. Batchelder, A. H. Zewail and T. Cole, *Appl. Opt.*, 1981, **20**, 3733-3754.
17. Y. Gu, X. Yao, H. Geng, G. Guan, M. Hu and M. Han, *ACS Appl. Mater. Interfaces*, 2021, **13**, 40798-40805.
18. T. Cai, J. Wang, W. Li, K. Hills-Kimball, H. Yang, Y. Nagaoka, Y. Yuan, R. Zia and O. Chen, *Adv. Sci.*, 2020, **7**, 2001317.
19. Y. Wang, Y. Liu, G. Xie, J. Chen, P. Li, Y. Zhang and H. Li, *ACS Appl. Mater. Interfaces*, 2022, **14**, 5951-5958.
20. A. R. Frias, M. A. Cardoso, A. R. Bastos, S. F. Correia, P. S. André, L. D. Carlos, V. de Zea Bermudez and R. A. Ferreira, *Energies*, 2019, **12**, 451.
21. P. Xia, S. Xu, F. Liu, Q. Lu, K. Yang, Z. Wang, Y. Cui, D. Ban and C. Wang, *Sol. RRL*, 2021, **5**, 2100491.
22. L. Zdrazil, S. Kalytchuk, M. Langer, R. Ahmad, J. Pospisil, O. Zmeskal, M. Altomare, A. Osvet, R. Zboril and P. Schmuki, *ACS Appl. Energy Mater.*, 2021, **4**, 6445-6453.
23. S. K. Hill, R. Connell, J. Held, C. Peterson, L. Francis, M. A. Hillmyer, V. E. Ferry and U. Kortshagen, *ACS Appl. Mater. Interfaces*, 2020, **12**, 4572-4578.
24. E. P. Merkx, M. P. Plokker and E. van der Kolk, *Sol. Energy Mater. Sol. Cells*, 2021, **223**, 110944.
25. Y. Zhao and R. R. Lunt, *Adv. Energy Mater.*, 2013, **3**, 1143-1148.
26. J. Choi, K. Kim and S.-J. Kim, *Sci. Rep.*, 2021, **11**, 13833.
27. S. Mattiello, F. Corsini, S. Mecca, M. Sassi, R. Ruffo, G. Mattioli, Y. Hattori, T. Kusamoto, G. Griffini and L. Beverina, *Materials Advances*, 2021, **2**, 7369-7378.
28. S. Mattiello, A. Sanzone, F. Bruni, M. Gandini, V. Pinchetti, A. Monguzzi, I. Facchinetti, R. Ruffo, F. Meinardi and G. Mattioli, *Joule*, 2020, **4**, 1988-2003.
29. M. J. Talite, H.-Y. Huang, K.-B. Cai, K. C. Capinig Co, P. A. Cynthia Santoso, S.-H. Chang, W.-C. Chou and C.-T. Yuan, *J. Phys. Chem. Lett.*, 2019, **11**, 567-573.
30. S. Han, G. Chen, C. Shou, H. Peng, S. Jin and C.-C. Tu, *ACS Appl. Mater. Interfaces*, 2020, **12**, 43771-43777.
31. J. L. Banal, J. M. White, T. W. Lam, A. W. Blakers, K. P. Ghiggino and W. W. Wong, *Adv. Energy Mater.*, 2015, **5**, 1500818.
32. C. Lee, H. Cho, J. Ko, S. Kim, Y. Ko, S. Park, Y. Kang, Y. J. Yun and Y. Jun, *Opt. Express*, 2022, **30**, 37085-37100.
33. J. Choi, D. Nguyen, E. Gi, K. A. Brylev, J. W. Yu, D. Kim, W. B. Lee, D. H. Kim, I. Chung and K. K. Kim, *J. Mater. Chem. C*, 2022, **10**, 4402-4410.
34. J. Huang, J. Zhou, E. Jungstedt, A. Samanta, J. Linnros, L. A. Berglund and I. Sychugov, *ACS Photonics*, 2022, **9**, 2499-2509.
35. S. Han, J. Wen, Z. Cheng, G. Chen, S. Jin, C. Shou, H.-C. Kuo and C.-C. Tu, *Opt. Express*, 2022, **30**, 26896-26911.
36. N. Byambasuren, A.-R. Hong, W.-Y. Lee, J. Y. Byun, G. Kang, H. Ko and H. S. Jang, *Sci. Rep.*, 2022, **12**, 17595.
37. Y. Wang, G. Xie, J. Chen, X. Zhang, C. Chen, J. Yin and H. Li, *J. Mater. Chem. C*, 2022, **10**, 11924-11930.